JOURNAL OF GEOPHYSICAL RESEARCH: ATMOSPHERES, VOL. 118, 8346–8358, doi:10.1002/jgrd.50651, 2013

Nighttime secondary ozone layer during major stratospheric sudden warmings in specified-dynamics WACCM

Olga V. Tweedy,[1,2] Varavut Limpasuvan,[1] Yvan J. Orsolini,[3,4] Anne K. Smith,[5] Rolando R. Garcia,[5] Doug Kinnison,[5] Cora E. Randall,[6,7] Ole-Kristian Kvissel,[8] Frode Stordal,[8] V. Lynn Harvey,[6,7] and Amal Chandran[9]

Received 26 March 2013; revised 5 July 2013; accepted 15 July 2013; published 9 August 2013.

[1] A major stratospheric sudden warming (SSW) strongly impacts the entire middle atmosphere up to the thermosphere. Currently, the role of atmospheric dynamics on polar ozone in the mesosphere-lower thermosphere (MLT) during SSWs is not well understood. Here we investigate the SSW-induced changes in the nighttime "secondary" (90–105 km) ozone maximum by examining the dynamics and distribution of key species (like H and O) important to ozone. We use output from the National Center for Atmospheric Research Whole Atmosphere Community Climate Model with "Specified Dynamics" (SD-WACCM), in which the simulation is constrained by meteorological reanalyses below 1 hPa. Composites are made based on six major SSW events with elevated stratopause episodes. Individual SSW cases of temperature and MLT nighttime ozone from the model are compared against the Sounding of the Atmosphere using Broadband Emission Radiometry observations aboard the NASA's Thermosphere Ionosphere Mesosphere Energetics and Dynamics (TIMED) satellite. The evolution of ozone and major chemical trace species is associated with the anomalous vertical residual motion during SSWs and consistent with photochemical equilibrium governing the MLT nighttime ozone. Just after SSW onset, enhanced upwelling adiabatically cools the polar region from 80 to 100 km and transports low H from below. These conditions promote a concentration increase in the secondary ozone layer. Subsequent downwelling from the lower thermosphere warms the MLT and enhances the descent of H from the thermospheric reservoir, thereby limiting the secondary ozone concentration increase. Negative correlation of secondary ozone with respect to temperature and H is more pronounced during winters with SSWs than during non-SSW winters.

Citation: Tweedy, O. V., et al. (2013), Nighttime secondary ozone layer during major stratospheric sudden warmings in specified-dynamics WACCM, *J. Geophys. Res. Atmos.*, *118*, 8346–8358, doi:10.1002/jgrd.50651.

1. Introduction

[2] A major sudden stratospheric warming (SSW) is a natural phenomenon that impacts the state of the atmosphere from the ground to 140 km in altitude [*Limpasuvan et al.*, 2004, 2005; *Kuroda*, 2008; *Karlsson et al.*, 2009]. Such dramatic SSW event originates from the interaction between the mean state and planetary waves of tropospheric origin that propagate upward to the middle atmosphere [*Matsuno*, 1971; *Holton*, 1976]. The damping of these planetary waves in the upper stratosphere induces a strong poleward residual motion that results in enhanced downwelling in the winter polar stratosphere (responsible for the rapid warming associated with SSW) and an enhanced upwelling in the winter polar mesosphere (and adiabatic cooling of the polar mesosphere). Subsequently, an SSW event occurs in conjunction with a sudden mesospheric cooling (SMC) phenomenon, as suggested by studies like *Siskind et al.* [2005, 2010].

[3] During SSW onset, the polar stratospheric winds switch from their typical eastward direction to an anomalous westward direction, indicating a breakdown of the vortex

[1]School of Coastal and Marine System Science, Coastal Carolina University, Conway, South Carolina, USA.
[2]Now at Department of Earth and Planetary Sciences, Johns Hopkins University, Baltimore, Maryland, USA.
[3]Norwegian Institute for Atmospheric Research, Kjeller, Norway.
[4]Birkeland Centre for Space Science, University of Bergen, Bergen, Norway.
[5]National Center for Atmospheric Research, Boulder, Colorado, USA.
[6]Department of Atmospheric and Oceanic Sciences, University of Colorado Boulder, Boulder, Colorado, USA.
[7]Laboratory for Atmospheric and Space Physics, University of Colorado Boulder, Boulder, Colorado, USA.
[8]Department of Meteorology, University of Oslo, Oslo, Norway.
[9]Geophysical Institute, University of Alaska Fairbanks, Fairbanks, Alaska, USA.

Corresponding author: O. V. Tweedy, Department of Earth and Planetary Science, Johns Hopkins University, Baltimore, MD 21209, Conway, SC 29528, USA. (otweedy1@jhu.edu)

2169-897X/13/10.1002/jgrd.50651

[*Labitzke*, 1981]. This stratospheric wind reversal filters out the westward gravity wave drag from reaching the lower mesosphere. Since westward gravity wave drag drives polar downwelling that helps maintain the stratopause and thermal structure of the mesosphere [*Hitchman et al*., 1989], its absence contributes to mesospheric cooling [*Siskind et al*., 2007].

[4] As SSW continues, the stratopause descends from the climatological position near 60 km toward the troposphere with the persistent upwelling (and cooling) aloft [*Limpasuvan et al*., 2012; *de la Torre et al*., 2012]. As documented by *Manney et al*. [2008], the stratopause sometimes reforms at an elevated altitude (~75–80 km) 2–3 weeks after the SSW onset before slowly returning to its original position [*Siskind et al*., 2007; *Randall et al*., 2009; *Hitchcock and Shepherd*, 2012]. The reformation of the elevated stratopause appears to be driven by the damping of a secondary planetary wave (wave number 1) in the MLT [*Limpasuvan et al*., 2012; *Chandran et al*., 2013a; *Tomikawa et al*., 2012]. The origin of this secondary planetary wave might be linked to *in situ* zonally asymmetric gravity wave breaking [*Manney et al*., 2008] or to a combination of forcing from below and *in situ* instability near/above the stratopause [*Siskind et al*., 2010; *Chandran et al*., 2013b].

[5] The reformation of the stratopause at an elevated altitude is accompanied by enhanced polar downwelling from the mesosphere-lower thermosphere (MLT) to the stratosphere, which readily transports chemical species. *Orsolini et al*. [2010], *Lee et al*. [2011], and *Kvissel et al*. [2012] found that enhanced downwelling due to SSW correlates with the presence of very dry mesospheric air, rich in carbon monoxide (CO), in the stratospheric polar region. Furthermore, *Randall et al*. [2005, 2006, 2009] reported the descent of high NO_x ($NO + NO_2$) related to strong downward motion during the SSW recovery phase. *McLandress et al*. [2012] suggested that nonorographic gravity wave drag plays an important role in driving the downward transport following the warming. Several recent studies also indicate significant impact of anomalous SSW dynamics on wintertime polar ozone in the MLT [*Sonnemann et al*., 2006; *Smith et al*., 2009; *Marsh*, 2011]. Climatologically, the polar nighttime ozone in this region exhibits a "secondary peak" near 90-105 km and a "tertiary peak" at 73 km. Similar to stratospheric ozone, which is a result of absorption of ultraviolet (UV) radiation (185–242 nm) by molecular oxygen, the "secondary" ozone maximum also forms by UV absorption at a much shorter wavelength (137 200 nm) [*Marsh et al*., 2001]. Very cold temperatures in the mesopause region and the location of the atomic oxygen density maximum allow for ozone peak at this altitude. Tertiary ozone maximum is a nighttime phenomenon found only in the wintertime hemisphere at high latitudes. This local maximum is caused by a relatively large decrease in destruction by hydrogen during nighttime conditions. While the secondary ozone peak nearly disappears in the daylight due to extremely fast photolytic destruction rate, the nighttime mixing ratio of ozone here is comparable to that found in the stratosphere [*Smith and Marsh*., 2005].

[6] *Sonnemann et al*. [2006] used the Leibniz-Institute Middle Atmosphere model to investigate the drastic aeronomic changes in the MLT region connected with a SSW at the end of January 2001. These authors found an intensification of both the secondary and the tertiary maximum of ozone and directly connected this rapid increase in concentration to very low temperatures and to the changing wind structure during the SSW. The authors also suggested importance of the vertical winds on the distribution of the water, atomic hydrogen, atomic oxygen, and other minor constituents important to ozone formation/depletion. However, a clear connection between vertical winds and the SSW event in contributing to secondary ozone variation was not made.

[7] Few years later, based on the Sounding of the Atmosphere using Broadband Emission Radiometry (SABER) observations aboard the NASA's Thermosphere Ionosphere Mesosphere Energetics and Dynamics (TIMED) satellite, *Smith et al*. [2009] suggested that SSW occurrence may (1) decrease the secondary ozone concentration and (2) vertically displace the tertiary ozone peak during the reformation of the stratopause. *Kvissel et al*. [2012] showed the deflection of the tertiary maximum as the SSW unfolds and a sharp decrease of the secondary ozone at the time of the stratopause reformation in a simulation with the National Center for Atmospheric Research (NCAR) Whole Atmosphere Community Climate Model (WACCM). These authors highlighted the importance of stratospheric dynamics in controlling the upper mesospheric structure and composition but pointed out the incomplete understanding of mesospheric ozone behavior.

[8] Presently, the nature of ozone variations in the MLT region during SSW events remains unclear. While previous studies and observations (see references above) allow us to infer chemical transport (transfer of minor chemical species by horizontal and vertical winds), the role of atmospheric dynamics on the ozone evolution in this altitude range remains unresolved. Satellite measurements of horizontal winds on the necessary time and spatial scales are not available and deriving vertical motion is difficult. In this paper, we investigate the change in MLT polar ozone due to SSWs by making a connection between dynamics, transport, and chemical composition based on results from nudged WACCM simulations. We focus particularly on the evolution of the secondary and tertiary peaks of wintertime polar ozone during SSWs by creating a composite representation of six major warming events, all of which are accompanied specifically by elevated stratopauses. These events are associated with changes in circulation over the polar cap. Along with satellite observations, we document a close relationship between the tertiary and secondary ozone layers. The same dynamical events that lead to the upward deflection of the tertiary ozone layer toward the mesopause during the onset of the SSW help account for the episodic increase in the secondary ozone layer concentration through adiabatic cooling and advection of air with low concentrations of atomic hydrogen. This increase subsides when downwelling in the MLT during the SSW recovery phase (which leads to the descent of an elevated stratopause) warms the secondary ozone layer. The behavior of the secondary ozone maximum largely follows photochemical equilibrium. By elucidating the enhancement of polar ozone near 100 km, our study provides a greater insight into the natural processes that govern MLT ozone variations.

2. Model Description and Methods

[9] For this study, we examined data from a "specified dynamics," or SD, WACCM4 (SD-WACCM) simulation, in which dynamics and temperature are nudged by reanalysis data in the lower part of the model domain. The specified meteorological fields come from the NASA Global Modeling and Assimilation Office Modern-Era Retrospective Analysis for Research and Applications (MERRA) [*Rienecker et al*., 2011]. In MERRA, temperature, zonal and meridional winds, and surface pressure are used to drive the physical parameterizations that control boundary layer exchanges, advective and convective transport, and the hydrological cycle. The WACCM meteorological fields are constrained by the MERRA meteorological fields using the approach described in *Kunz et al*. [2011]. This constraint is applied at every model time step (i.e., every 30 min). Consistent with a 50 h relaxation time constant, 1% of the MERRA fields were used every time step. For the meteorological fields, this scheme is applied from the surface to approximately 50 km (0.79 hPa); above 60 km (0.19 hPa), the model meteorological fields are fully interactive, with a linear transition in between.

[10] Covering 1980–2010, the SD-WACCM simulation has a horizontal resolution of $1.9° \times 2.5°$ (latitude longitude) with a vertical domain extending from the ground up to 150 km (88 vertical levels). The model's chemistry of the atmospheric region above 20 km is simulated by using a chemical scheme that includes the oxygen (O_3, O, $O(^1D)$), nitrogen (N, N (^2D), NO, NO_2, NO_3, N_2O_5, HNO_3, HO_2NO_2), hydrogen (H, OH, HO_2, H_2O_2), and halogen (ClO_x and BrO_x) families, an *E* region ionosphere, and excited species (N^+, N_2^+, NO^+, O^+, O_2^+). Given specified initial conditions, WACCM4 subsequently predicts the climate based on the relevant physical and chemical governing equations and climate simulations are expected to reproduce climate accurately [*SPARC*, 2010].

[11] This SD version of WACCM leads to an improved representation of the observed atmospheric dynamics and temperature for an individual year, compared to its free running counterpart. *Hoffmann et al*. [2012] compared SD-WACCM polar stratospheric and mesospheric CO with data from ground-based microwave radiometry for Arctic winters of 2008–2009 and 2009–2010. These authors showed good agreement of the model results with measurements in this region.

[12] Changes in dynamics and chemical species related to SSWs can fluctuate widely in strength (due to nonlinear, wave-mean flow interactions) and timing (since major SSWs occur at different times throughout a winter). To develop a statistically robust picture of the SSW characteristics, we perform a composite analysis based on six SSW cases simulated in SD-WACCM from 1990 onward (1997–1998, 2001–2002, 2003–2004, 2005–2006, 2008–2009, and 2009–2010). Every warming event is characterized by an elevated stratopause associated with changes in circulation over the polar cap; we thus refer to these events as "Elevated Stratopause" SSWs, or "ES-SSWs." Case-by-case examination of these events suggests similar anomalies in dynamics and ozone profiles during the stratopause descent and its reformation.

[13] Figure 1 shows zonal-mean zonal wind altitude-time series for these selected cases, averaged from 70 N to 90 N with star symbols (*) indicating the stratopause height. Major SSWs are identified based on the World Meteorological Organization (WMO) definition. The elevated stratopause is defined according to the method described by *de la Torre et al*. [2012] in which the stratopause is determined as the height of maximum temperature in the vertical range from 20 to 100 km. If the change in altitude of stratopause is greater than 15 km from its position on the previous day, the stratopause is elevated.

[14] For the purposes of this study, we define the "onset date" of a SSW as the time when the wind at 1 hPa (~50 km) reverses from eastward (solid contours) to westward (dotted contours shaded in gray) and persists for at least 5 days. While somewhat subjective, and different from the WMO definition of a major SSW, this onset date corresponds to the day when the polar wind reverses direction over an extended range of altitude in the mesosphere (50–80 km; as shown in Figure 1) and to the onset of anomalous vertical upwelling in the composite (as shown in Figure 2).

[15] Figure 1 shows that the onset dates (day 0) identified for all cases fall between late December and late January. To account for the different timing of the warming events, we shift the data with respect to the selected onset date. The SSW life cycle is defined to be 70 days long, from day −30 to day +40. Days with negative and positive values indicate the time prior to and after the SSW onset. The composite then combines and averages all of the aligned six ES-SSW events based on these life cycle days. All results of this study are given as a function of log-pressure altitude, with a fixed scale height of 7 km.

[16] In agreement with observations, six SSWs appear in the Northern Hemisphere winters of 1997–1998, 2001–2002, 2003–2004, 2005–2006, 2008–2009, and 2009–2010. We examine individual SSW cases of SD-WACCM with respect to SABER observations. *Smith et al*. [2009] describe SABER ozone and temperature in detail. In constructing the altitude-time plots, the SABER vertical profiles are filtered to remove unrealistic high ozone values, according to Chauvenet's criterion [*Taylor*, 1997]. This statistical test eliminates suspicious points if the probability of obtaining the particular deviation is less than $1/2n$ (where n is a total number of measurements in a sample).

3. SSW Composite Dynamical and Chemical Evolution

[17] Figure 2a shows the composite zonal-mean temperature (filled contours) and zonal-mean zonal wind (line contours) averaged from 70°N–90°N. Prior to SSW onset (day 0), eastward winds (solid contours) dominate below 80 km while westward winds (dashed contours) are present above 80 km. During the SSW, this wind pattern switches and persists for at least 10 days. With the wind reversal, the polar middle stratosphere (from 20–50 km) undergoes a sudden warming of 10–20 K in a few days, concurrent with mesospheric cooling aloft (blue region). The stratospheric warming is tied to the descent of the warm stratopause from 60 km to 40 km (shown by star symbols) beginning around day −5. With the recovery of eastward winds in the upper

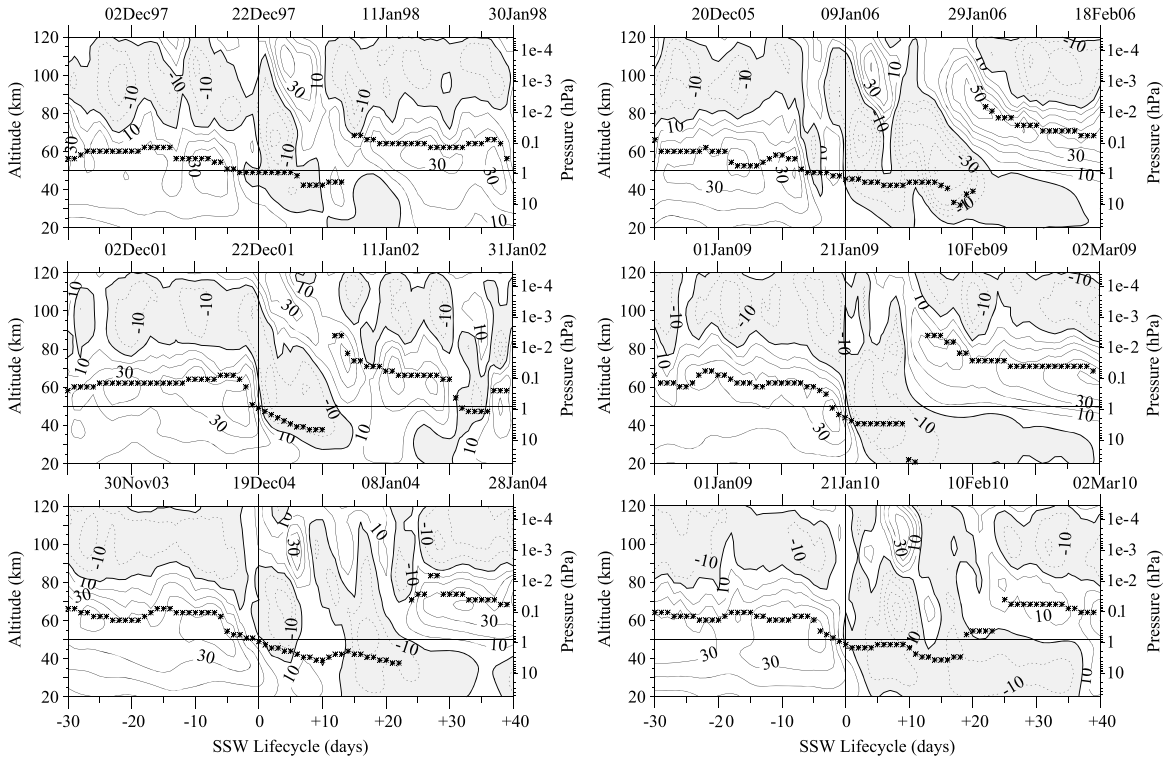

Figure 1. Zonal-mean zonal wind (U) averaged from 70°N to 90°N (contoured every 10 m s^{-1}) with eastward wind as solid lines and westward wind as dotted contours (and shaded). The stratopause location (height of maximum temperature between 20 and 100 km) is indicated by the star symbols. The bottom abscissa shows the SSW life cycle in days and the top abscissa the corresponding dates. Intersection of vertical and horizontal straight lines shows that day 0 corresponds to the date when U at 50 km switches from eastward to westward direction and persists for at least five consecutive days.

stratosphere and mesosphere by day +20, a new stratopause is reformed at higher altitude (~75 km) than before the SSW.

[18] The vertical residual motion in the polar cap is greatly altered as a consequence of SSW. Figure 2b shows the altitude-time evolution of the vertical component of the residual circulation (w*). In particular, the stratopause evolution noted above is associated with wintertime polar descent (solid contours). The persistently strong downwelling pattern from 60 to 80 km prior to day −5 promotes adiabatic warming that maintains the underlying stratopause. As suggested by *Hitchman et al*. [1989], breaking of westward gravity waves in the middle polar mesosphere caps the eastward jet near 80 km and drives this strong downwelling. After the onset of the SSW (day 0), the downwelling pattern moves to lower altitudes (along with the stratopause) as the stratosphere warms and the polar wind switches direction. Between day 0 and day +5, a region of relatively strong upwelling from 60 to 100 km (light gray area enclosed by thick zero contour) promotes adiabatic cooling in the overlying mesosphere and leads to the low temperature noted in Figure 2a during this time. The upwelling of about 8 mm s^{-1} is followed by the cooling of ~10 K day^{-1} between 80 and 100 km. This upwelling is attributed in part to a change in gravity wave drag (from westward to eastward forcing) due to the filtering effect of the underlying westward stratospheric wind during the SSW [*Siskind et al*., 2007]. A region of intense downwelling appears in the lower thermosphere around day +5 and descends toward the upper mesosphere during the next 30 days. The reformation of the stratopause at an elevated altitude appears about day +20, in conjunction with this strong downwelling.

[19] The above presentation of temperature, zonal wind, and w* agrees well with the major SSW composites of *de la Torre et al*. [2012]. These authors analyze 18 cases with ES-SSW in WACCM 3.5 (a free-running model) and define a central date corresponding to the time when the elevated stratopause in the mesosphere is detected. The time and location of the stratopause reformation differ from those of major SSW onset defined here. They note that major SSWs are not always associated with an elevated stratopause. In our study, all major SSW cases selected for our composite exhibit an elevated stratopause, which appears between 15 and 25 days after the zonal wind switches direction over the polar cap (Figure 1). Consequently, our definition of the central day of the composites does not alter the overall composite characteristics when compared to *de la Torre et al*. [2012]. However, upwelling produced prior to the stratopause reformation in our SD-WACCM composite extends to much higher altitude (~100 km) compared to the free running counterpart (~85 km). The difference between w* in composites is more likely due to the criteria adopted to define day 0 and to number of cases used to produce the composites, and less likely due to the differences in models.

[20] Figures 2c–2f illustrate the composite evolution of nitrogen oxides (NO_x), nighttime ozone (O_3), atomic oxygen (O), and hydrogen (H), respectively during the ES-SSW.

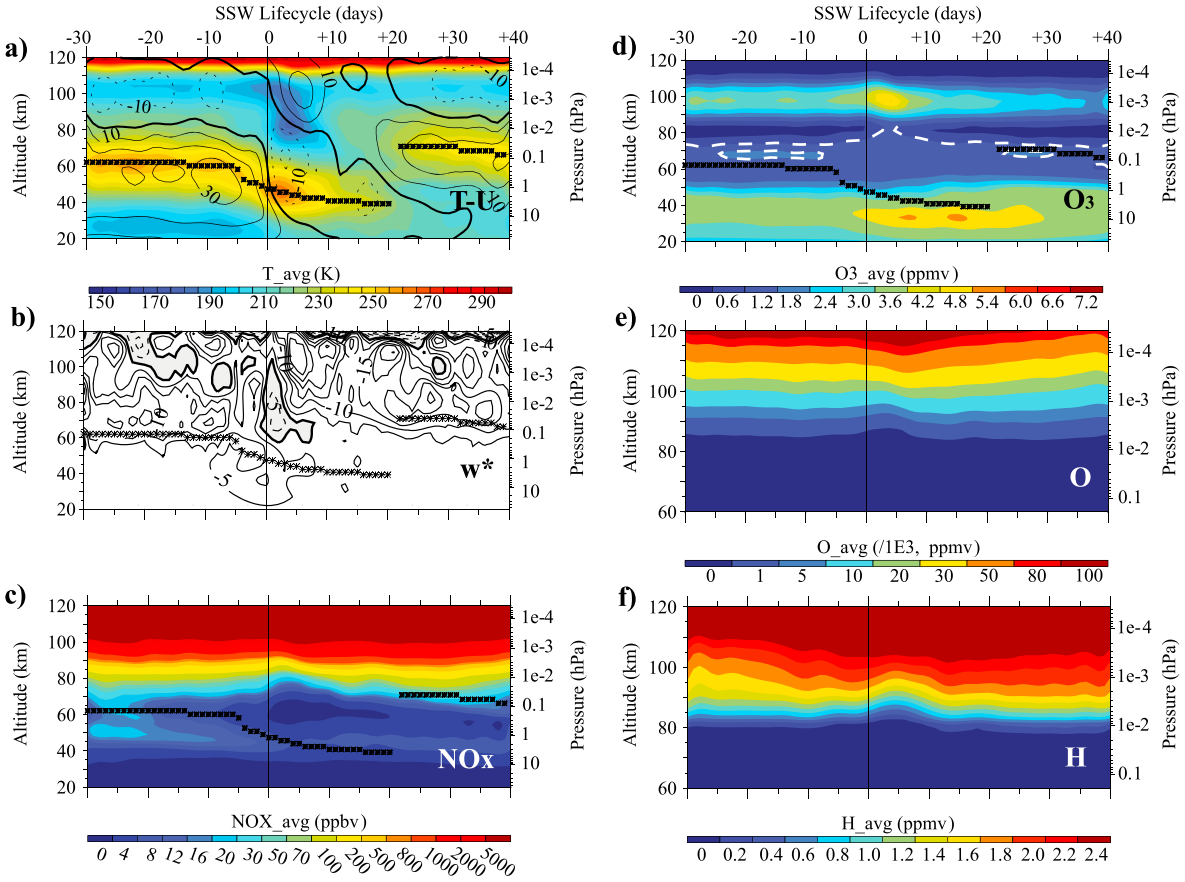

Figure 2. Zonal-mean ES-SSW composite. (a) Temperature (filled contours) in degree K and zonal wind (line contours) in m s^{-1}. (b) Vertical residual circulation (w^*) contoured every 5 mm s^{-1} with upwelling (as dashed contours and shaded) and downwelling (as solid contours). (c) Nitrogen oxides (NO_x) in ppbv. (d–f) Nighttime O_3, atomic O, and atomic H in ppmv. Each composite is averaged from 70°N to 90°N and consists of six ES-SSW events. In ozone, the 1.2 and 1.8 ppmv contours are shown in white to illustrate the tertiary maximum layer. Star (*) symbols indicate the stratopause location. The abscissa shows the SSW life cycle in days (with day 0 being the SSW onset).

The evolution of H and that of O are shown only in the vertical range of 60 km to 120 km since their volume mixing ratios below 60 km are negligible. Overall, the evolution of these tracers appears well connected with the vertical residual motion shown in Figure 2b. Figure 2d shows that, just after SSW onset, the tertiary ozone layer near 70 km (outlined by the white dashed contours) is deflected upward by nearly 10 km as in *Kvissel et al*. [2012], and the volume mixing ratio of the secondary ozone at 90–100 km rapidly increases as noted by *Sonnemann et al*. [2006], coincident with the upwelling that occurs during the wind reversal. This uplifting is also apparent in the deflection of O, H, and NO_x as their isopleths become more closely spaced in the altitude range from 70 to 100 km. Five to seven days later, the tertiary ozone maximum descends to its pre-SSW altitude and the secondary ozone maximum decreases in volume mixing ratio, coincident with intense downwelling in the thermosphere around day +10. The persistently strong downwelling is reflected in the NO_x rich air penetrating downward and across 70 km with the descent of the reformed stratopause (around day +20). Although NO_x does not participate in the chemical destruction or formation of ozone at this altitude, its time series serves as an indicator of the residual vertical motion. However, the horizontal transport and high solar activity can greatly affect the behavior of this chemical tracer and, therefore, should be taken into consideration.

[21] Overall, the composite SSW dynamical evolution and life cycle shown here are consistent with satellite observations [*Manney et al*., 2008; *Orsolini et al*., 2010] and other global climate model simulations [*Limpasuvan et al*., 2012; *Hitchcock and Shepherd*, 2012; *Chandran et al*., 2013a]. These robust wind, temperature, and vertical velocity composite patterns represent the "typical" picture of a SSW (as opposed to individual events in case studies). The strong descent of the composite tracers a few weeks after SSW onset is also consistent with observations. For example, using data from the Atmospheric Chemistry Experiment Fourier Transform Spectrometer satellite instrument, *Randall et al*. [2009] found NO_x mixing ratios in years with a substantially elevated stratopause to be a factor of 2 to 20 higher at 55 km level than during non-SSW years.

4. The Secondary Ozone Layer During SSW

[22] To focus on the mesopause ozone layer, Figure 3 shows the composite time series of the secondary ozone

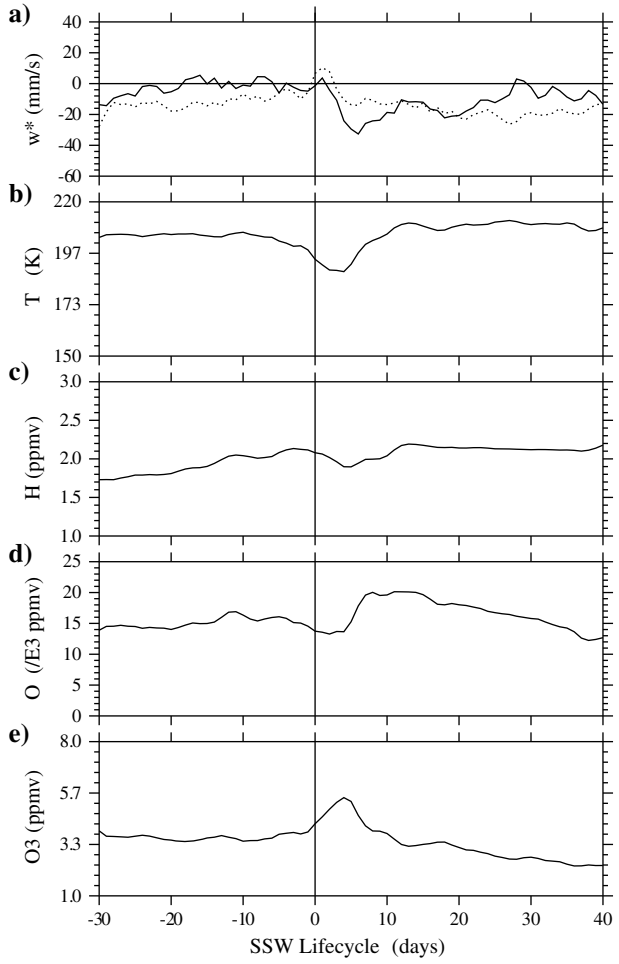

Figure 3. ES-SSW composite time series of (a) zonal-mean w^*, (b) T, (c) H, (d) O, and (e) nighttime ozone, and averaged from 70°N to 90°N at 97 km. w^* is shown for 97 km (solid line) and for 80 km (dotted line) levels. Volume mixing ratio of O is scaled by 1000.

maximum, temperature, and w^* along with other chemical species important for ozone (H and O). Every time series is made at log-pressure altitude of 97 km. In addition, w^* is also shown at 80 km level (dotted line) because vertical wind and temperature tend to be in temporal quadrature. As expected, the time evolution follows the characteristics at 97 km shown in Figure 2. In particular, near the onset date, mesospheric upwelling, which is stronger at 80 km level, leads the rapid cooling in the MLT and the ozone enhancement between day 0 and day +6. The subsequent intense downwelling corresponds to the decline in ozone. This downwelling is much stronger at 97 km.

[23] The time rate of change of temperature correlates very highly with w* and maximizes as the period of vertical motion subsides; consequently, the greatest vertical displacement tends to occur when the vertical motion is done. Therefore, the updraft precedes the temperature minimum by a few days, but the rate of temperature decrease is strongest when the updraft is strongest.

[24] During the polar night conditions, atmospheric motion greatly influences the distribution of O and H in the MLT region above 90 km. Atomic oxygen exhibits low mixing ratios at day 0, followed by a rapid increase a few days later and a slow decrease thereafter. The strong correlation of O with w^* exists because O is the dominant and long lived species at 90–100 km. Atomic hydrogen behaves similarly to O and also declines 2 days after the upwelling and increases during strong downwelling.

[25] The above composite time series provide a robust picture of the secondary ozone layer evolution during SSW. While similar secondary ozone enhancement is seen within 10 days of SSW onset in nearly all SSW cases with an elevated stratopause, the amount of ozone increase and exact timing for the individual cases differs slightly from the "typical" composite behavior. Also, due to the high variability in data above 80 km, the composite w^* does not show evidence of upwelling stronger than 5 mm s^{-1} between 90 and 100 km prior to the stratopause reformation. Nevertheless, individual ES-SSW cases from SD-WACCM indicate much stronger upward velocities at this altitude a few days prior to the temperature decrease.

[26] For instance, Figure 4 shows altitude-time series of w^* averaged over 70–90°N for the 2010 case. Similar to the composite, prior to day 0, very strong downwelling extends to the lower altitudes along with the stratopause and reappears in the lower thermosphere at day +10. However, uncharacteristic upwelling, present between day −5 and day +10, exceeds 20 mm s^{-1} from 80 to 100 km level. The magnitude and duration of this ascent generate significant cooling of this region. Time series for this SSW are shown in Figure 5. The strong ozone enhancement on day +8 coincides with a sharp decline in temperature and H, indicative of prior upwelling from lower altitudes between day +2 and day +10. With this upwelling, the atomic O also decline since this species rapidly decreases in concentration below 90 km. The upwelling is replaced, after about day +7, by strong descent from the lower thermosphere that accompanies the reformation of the stratopause. The associated disparity in vertical residual circulation accounts for differences in temperatures and volume mixing ratios of H and O between this individual year and the composites discussed previously. Overall, the 2010 case shows that during SSW onset, the secondary ozone maximum (around day +8 between 90 and

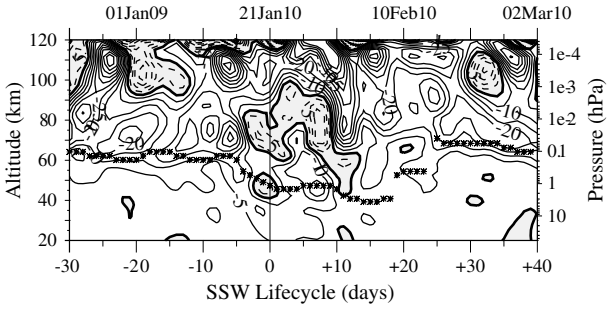

Figure 4. Zonal-mean vertical residual circulation (w^*) for 2010 ES-SSW case simulated in SD-WACCM. Values are contoured levels every 5 mm s^{-1} upwelling (as dashed contours and shaded) and downwelling (as solid contours). The star (*) symbols indicate the stratopause location. The bottom abscissa shows the SSW life cycle in days (with day 0 being the SSW onset), and the top abscissa shows corresponding dates.

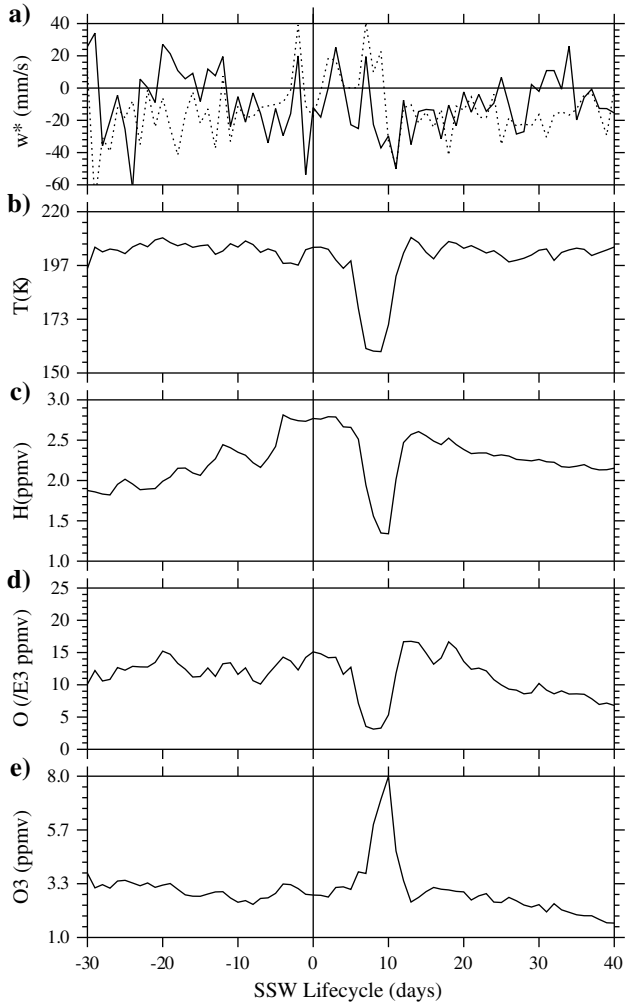

Figure 5. Time series of (a) zonal-mean w^*, (b) T, (c) H, (d) O, and (e) nighttime ozone, averaged from 70°N to 90°N at 97 km level for 2010 SD-WACCM with day 0 corresponding to 22 January 2010. w^* is shown for 97 km (solid line) and for 80 km (dotted line) levels. Volume mixing ratio of O is scaled by 1000.

100 km) responds to prior upwelling from lower altitudes, followed by a subsequent downwelling from higher altitudes (as shown in Figures 4 and 5).

[27] The dramatic changes in secondary ozone mixing ratios in the 2010 case are illustrated in Figure 6, which shows polar maps of key species (O_3, O, H, and T) at 97 km for 2 days. These days corresponding to 23 January (day +2) and 31 January (day +10) capture the distribution of these species before and during the intense ozone peak. The sunlit portions of the ozone plots are shown in black because daytime ozone is much smaller than nighttime. Consistent with the time series in Figure 5, the distribution of all species on day +2 (Figure 6a) is highly homogeneous and the vortex is ill-defined; the atomic O mixing ratio is near 10^4 ppmv while O_3 is between 2 and 3 ppmv. The H volume mixing ratios are above 2.4 ppmv, and the temperature is near 200 K.

[28] Upwelling between day +2 and day +6 changes the situation dramatically. By day +10 (Figure 6b) when downwelling is again dominant, coherent polar structures are evident in all species. Over the polar region, the temperature is less than 160 K and ozone exceeds 8 ppmv, consistent with the time series of Figure 5. The volume mixing ratios of H and O are also significantly lower than the values 8 days earlier, and the vortex is well defined. Nine days later (not shown), the distributions of these species are again nearly homogeneous, as on day +2. Polar maps of chemical species and the shape of vortex indicate very strong upwelling prior to temperature decrease and ozone intensification. They also suggest that most upwelling occur poleward of 70°N. This upwelling is a major mechanism of a rapid mesospheric cooling and decrease in concentration of H and O, which occurs few days later.

[29] *Smith et al*. [2008, 2009, 2010, 2011] described the formation mechanism of the secondary ozone maximum in detail. Briefly, atomic oxygen (O) and molecular oxygen (O_2) combine to form ozone. The main losses of ozone in polar night conditions are due to reactions involving atomic hydrogen (H) as well as atomic oxygen (O). However, the reaction of O with O3 composes just ~10% of nighttime ozone loss [*Smith et al*., 2008]. Thus, the reaction involving O dominates ozone production and the reaction involving H dominates ozone loss at this altitude.

[30] According to *Smith et al*. [2009], the secondary ozone layer during polar night is nearly in photochemical equilibrium, which assumes that losses of O_3 by the reaction with H and O are in balance with the production from the reaction involving $O + O_2$. In this balanced state, the secondary maximum ozone density is given by

$$[O_3] = \frac{k_1[O][O_2]n}{k_2[O] + k_3[H]} \tag{1}$$

$$k_1 = 6.0 \times 10^{-34}(300\,\mathrm{K}/T)^{2.4} \tag{2}$$

$$k_2 = 8.0 \times 10^{-12} e^{(-2060\mathrm{K}/T)} \tag{3}$$

$$k_3 = 1.4 \times 10^{-10} e^{(-470\mathrm{K}/T)} \tag{4}$$

[31] Here, the quantities in brackets represent concentrations (molecules cm^{-3}), and n is the density of air. The reaction coefficients (k_j, $j = 1, 2, 3$), the densities of the various species, and n are all temperature (T) dependent. Density on a pressure surface is inversely proportional to temperature. The coefficient k_1 decreases with temperature while k_2 and k_3 increase with temperature. As a result of these dependences, nighttime photochemical equilibrium ozone at the secondary maximum decreases strongly with increasing temperature.

[32] Figure 7 shows the secondary ozone budgets at 97 km level for winter of 2009–2010. Ozone mixing ratios taken directly from the model (Figure 7a) and calculated according to equation (1) at 97 km level (Figure 7b) are nearly identical during the SSW life cycle. Very close correspondence in ozone mixing ratios at this altitude demonstrates that the secondary ozone layer in SD-WACCM during SSW life cycle is in photochemical equilibrium. Figures 7c–7e show additional estimates of ozone computed to investigate the role of atomic H, O, and temperature in ozone formation. Their mean values are calculated over the time of SSW life cycle (from day −30 to day +40) when ozone is in photochemical equilibrium at 97 km level. With H, T, and O set to their

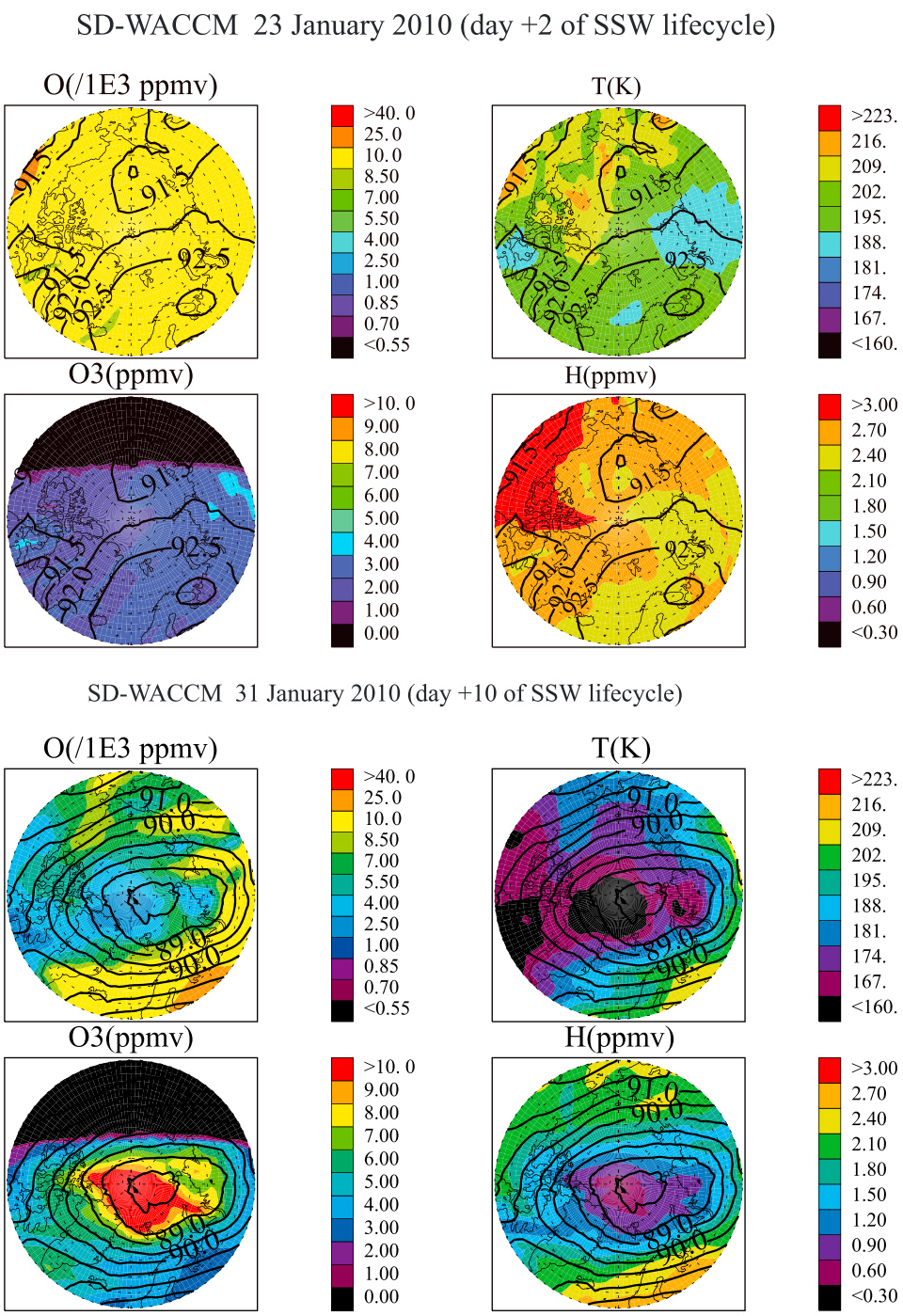

Figure 6. (a) SD-WACCM polar stereographic maps of key species at 97 km (where the secondary ozone maximum occurs) at Day +2 (23 January 2010) of SSW life cycle. The vortex shape is indicated by geopotential height (black contours, in km) with contour levels every 500 m. (b) Same as Figure 6a except for Day +10 of SSW life cycle corresponding to 31 January 2010.

average value (2.25 ppmv, 200 K, and 11.5×10^3 ppmv, respectively), the calculated ozone is nearly constant (not shown). By using H from the model (as shown in Figure 5c) while fixing *T* and O (Figure 7c) to their mean values, we observe an increase in ozone, which is attributed to the rapid decrease in H during strong upwelling in this region. Although varying H produces ozone peak at the same time as in Figure 7b, the magnitude of the increase is much smaller; therefore, additional factors must also contribute to ozone formation. Similarly, Figure 7d shows the effect of atomic O (as shown in Figure 5d) during constant temperature and H. The O_3 decrease in this estimate coincides with a decrease in O during the same time interval, indicative of a positive relationship between these species, consistent with (1). The largest effect on ozone among three tested variables is obviously produced by the temperature. With fixed H and O, Figure 7e indicates that variation in temperature (as shown in Figure 5b) leads to the largest increase in ozone mixing

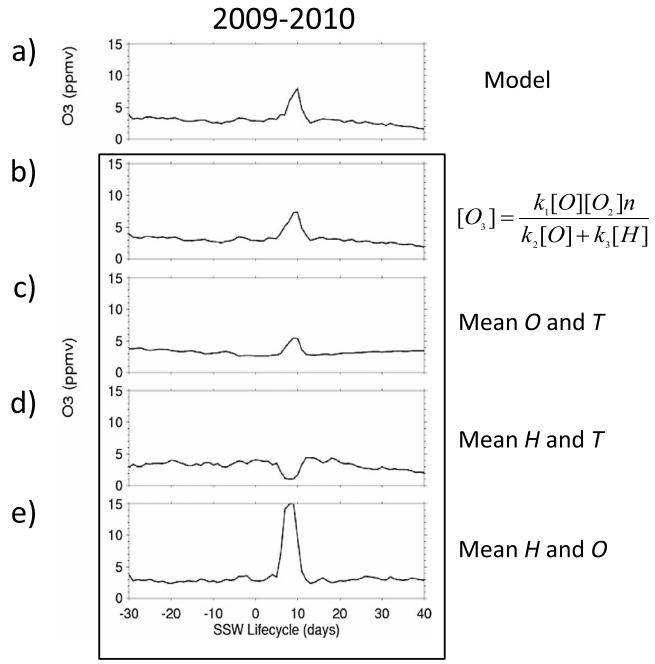

Figure 7. (a) Zonal-mean nighttime ozone averaged between 70°N and 90°N at 97 km provided by 2009–2010 SD-WACCM. (b) Same as Figure 7a but O_3 budget is computed assuming equilibrium and using H, O, and temperature from SD-WACCM; (c) the same as Figure 7b but with *T* and O set to a mean values indicating the importance of H; (d) the same as Figure 7b but with *T* and H are set to mean values showing the effect of O; (e) O and H are constant mean values with varying *T*. The mean values for O (11.5×10^3 ppmv), *T* (200 K), and H (2.25 ppmv) are calculated between day −30 and day +40 of SSW life cycle.

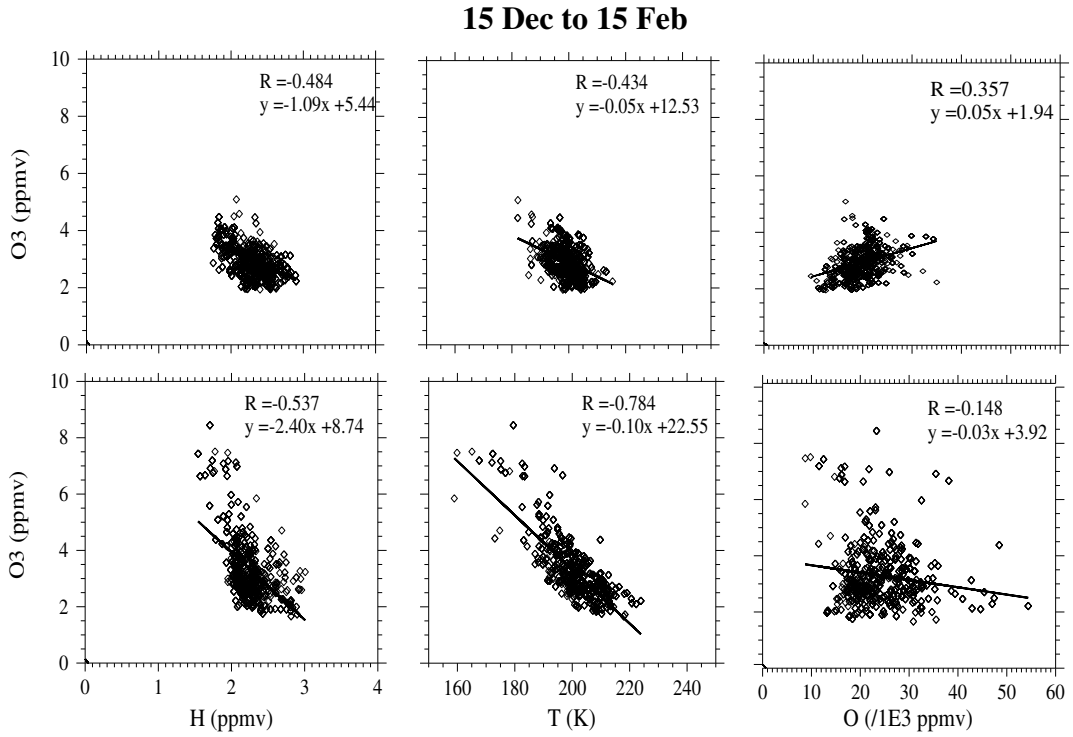

Figure 8. Correlation between (left column) zonal-mean nighttime ozone and H, (middle column) temperature, and (right column) O for (top row) six selected winters with ES-SSW and (bottom row) six winters without ES-SSW in SD-WACCM model. All values are averaged between 90 and 100 km and from 70°N to 90°N from 15 December to 15 February of each winter.

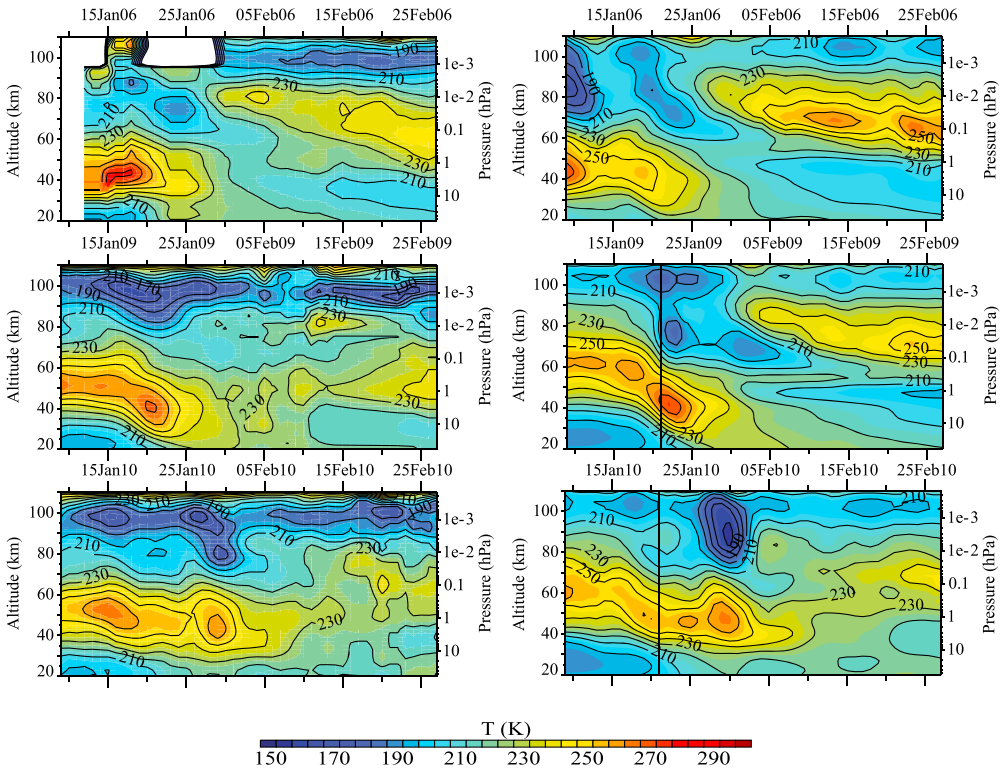

Figure 9. Zonal-mean temperature from SABER (left) and SD-WACCM (right) averaged between 70°N and 90°N. The vertical line on the SABER and SD-WACCM plots indicate the SSW life cycle Day 0. In SABER, vertical levels are given as tangent-point altitude (km), and in SD-WACCM are given as log-pressure altitude (km).

ratio compared to the estimate of Figure 7b. The rapid decrease in temperature following mesospheric upwelling accelerates the production of the secondary ozone.

[33] When computing and comparing reaction rates for 200 K versus 150 K, k1 is twice as big, k2 is 1/32 as big, and k3 is almost half as big at 150 K than at 200 K. Due to the difference in the reaction rates, one would expect 4 times the nighttime ozone amount produced at 150 K than at 200 K, as shown in Figure 7e. However, the ozone increase seen in Figure 7a is not as large (4×) and the sum of time series shown in Figures 7c–7e does not necessarily correspond to the total estimate presented in Figure 7b because of the nonlinearity of equation (1) and loss by atomic oxygen. Negative correlation with *T* and H in 2010 case (Figure 5) is consistent with the equilibrium ozone predicted by equation (1). The behavior of secondary ozone between day 0 and day +10 is attributed to the strong decrease in *T* and H, which act to decrease equilibrium ozone. We note here that *temperature plays a major role* in ozone formation, and the change in O_2 mixing ratio is negligible in determining the secondary ozone budget. The described relationships of ozone at the secondary maximum with H, O, and *T* are only valid during nighttime conditions. During daylight, photodissociation overwhelms three-body production and the additional, much faster, loss of ozone by photolysis must be included.

[34] The relationship between nighttime secondary ozone and temperature, atomic oxygen and hydrogen can also be readily seen in one-to-one correlation plots shown in Figure 8. Here the correlation is composed of all data from the six cases included in the composite (for the time period of 15 December and 15 February). The data are zonally averaged from 70°N to 90°N within the 90–100 km layer; for comparison, we also show similar data from six other winter seasons (for the same time period) without ES-SSW. The vertical profiles of these non-SSW winters in SD-WACCM (1992–1993, 1995–1996, 1996–1997, 1999–2000, 2004–2005, 2006–2007) do not show any changes in circulation or reformation of the stratopause often associated with warming events.

[35] SSW winters (top row) clearly illustrate the negative correlation between ozone and both temperature and H. The illustrated negative correlation is consistent with the idea that mesospheric upwelling promotes mesospheric cooling which enhances ozone at the secondary maximum and thermospheric downwelling inhibits that enhancement. We note, in particular, that this negative relationship is much more pronounced in SSW winters than in non-SSW winters (bottom row). The correlation between nighttime ozone and atomic O is positive during non-SSWs (right column), in agreement with *Smith et al*. [2009]. The budget analysis indicates the positive relationship of O with ozone and is consistent with non-SSW scatterplots (not shown).

[36] However, during ES-SSW seasons, the anomalous circulation results in a strong upward motion of low atomic oxygen air from below; this relationship alters and ozone becomes negatively correlated to O. At this time of very strong upwelling, the impact of O on the secondary ozone maximum during SSWs under the equilibrium assumption is minimum (Figure 7d). Given the very cold temperature

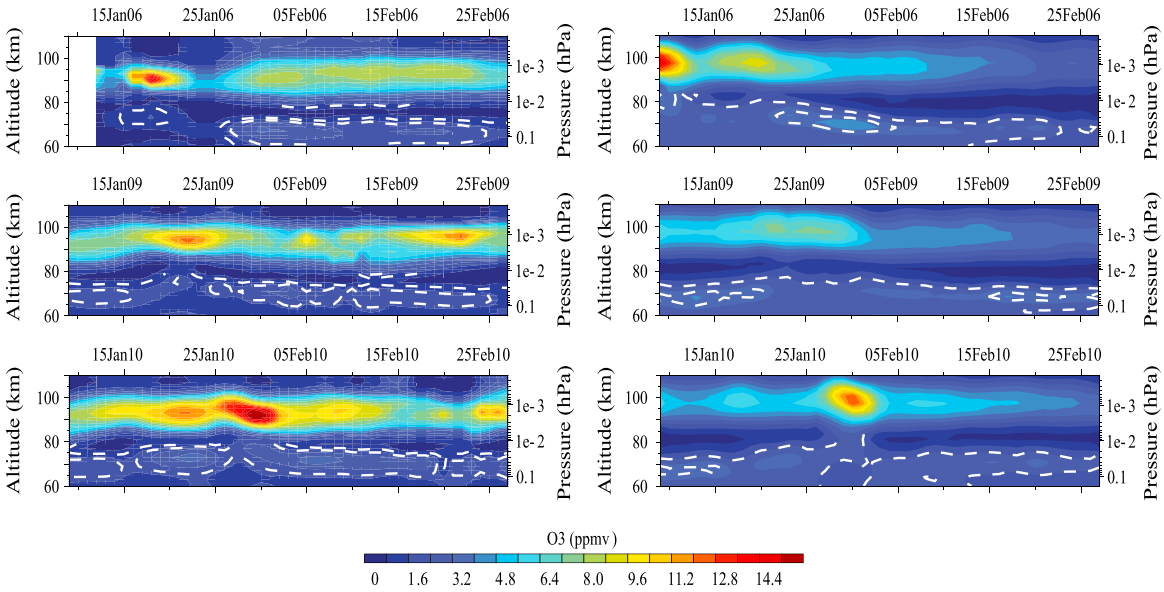

Figure 10. Zonal-mean nighttime ozone from SABER (left) and SD-WACCM (right) averaged between 70°N and 90°N. Note, ozone values in SD-WACCM are multiplied by a factor of two to keep the same color bar. The 1.2 and 1.8 ppmv isopleths are shown in white to illustrate the tertiary maximum layer. The actual dates are provided on the top abscissas. In SABER, vertical levels are given as tangent-point altitude (km) and in SD-WACCM are given as log-pressure altitude (km).

and a sharp decline in H, which follows mesospheric upwelling during SSW, small O mixing ratios do not contribute significantly to the overall ozone decrease. As a result, the SSW scatterplot indicates an increase in ozone corresponding to the decrease in O. Overall, we tend to see an inverse relationship between O_3 and H, and between O_3 and temperature in accordance with the equilibrium equation (1). These relationships are also seen in the composite (Figure 3).

5. Comparisons With Observed Ozone at the Secondary Maximum

[37] Since SD-WACCM is constrained by the MERRA reanalyses, the simulated ES-SSW events occur at about the same time as in the observations. The right columns of Figures 8 and 9 show the altitude-time cross sections of SD-WACCM zonal-mean temperature and nighttime ozone, respectively (averaged from 70°N to 90°N) for three SSW events that occurred in the winters of 2005–2006, 2008–2009, and 2009–2010 (see Figure 1 for date of the SSW onset). For comparison, the corresponding left columns show the temperature and nighttime ozone from SABER observations for the same time as in SD-WACCM. Here, the SABER profiles poleward of 70°N are binned together for each date. Since the mesopause ozone values in SABER is near twice the SD-WACCM amount, SD-WACCM ozone is multiplied by two in Figure 10 to keep the same color bar as for SABER. For 2006, 2009, and 2010, the observed SSW occurs nearly at the same time as in the model. In all cases, the cross sections (from 9 January to 28 February) exhibit the stratopause behavior much like the composite in Figure 2. The stratopause initially descends toward the stratosphere with SSW onset. Then, a new stratopause is formed at an elevated altitude before descending back toward its pre-SSW level. The tertiary ozone layers (Figure 10), highlighted by the white dashed contours (1.2 and 1.8 ppmv), are deflected upward toward 85–90 km a few days after the SSW onset, in concurrence with the secondary ozone concentration increase near 95 km. As documented by *Smith et al.* [2009], using SABER data, the winter of 2003–2004 also experienced a major SSW event with an elevated stratopause. However, the warming occurred in early January, before the start of SABER's northward-looking yaw cycle; therefore, SABER observations at high latitudes began only after the reformation of the stratopause at elevated altitude and neither mesospheric cooling nor intensification of ozone can be seen in this case and directly compared to SD-WACCM.

[38] While the timing of the simulated intensification of the secondary ozone layer near 95–100 km layer is consistent with the observations, SABER ozone mixing ratio at the secondary maximum is nearly twice larger than the predicted

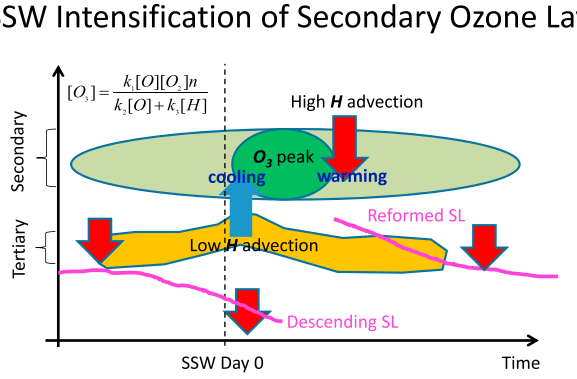

Figure 11. A schematic summary of the processes involved in the intensification of nighttime secondary ozone maxima during a major SSW with an elevated stratopause (SL).

SD-WACCM. SD-WACCM mesopause temperatures (around 90–110 km) are warmer on average by 5–10 K, and mesospheric cooling reaches much lower altitudes during the stratopause descent than SABER. Also, the reformed stratopause produced by SD-WACCM is much warmer which would indeed lead to a lower O_3 concentration. The reasons for these discrepancies are yet unclear and warrant further investigation. A problem may be the model's treatment of vertical diffusion and parameterized gravity wave drag.

6. Summary

[39] Six SD-WACCM simulations of ES-SSW events are examined with respect to the evolution of the nighttime secondary ozone layer in the MLT region. Composites with respect to the SSW life cycle are made, along with comparisons to individual cases from specified-dynamics simulations. During SSWs, the atmospheric dynamics and chemistry become highly perturbed relative to climatology, resulting in significant changes in ozone and chemical trace gases like NO_x, O, and H [*Smith et al*., 2010; *Kvissel et al*., 2012; *Smith*, 2012].

[40] Consistent with previous studies (referenced in section 1), anomalous vertical (residual) velocity episodes are evident in the ES-SSW composite between the altitude of 20 and 120 km in the polar region. (1) Few days prior to SSW onset, downwelling extends to the lower altitudes reaching 20 km a week later. (2) Immediately, after the wind reversal in the stratosphere, strong upwelling (uncharacteristic for this time and region) appears in the mesosphere between 60 and 100 km and persists for up to 7 days. (3) Strong downwelling from the thermosphere appears 2–4 days after SSW onset, then, a few days later, extends to the middle mesosphere replacing the mesospheric upwelling.

[41] Figure 11 summarizes the conclusions drawn from this study. In agreement with *Smith et al*. [2009] and [*Marsh*, 2011], the tertiary ozone layer is directly affected by upwelling due to a long photochemical lifetime of ozone below 80 km during the polar night. As part of the mesospheric cooling during SSW, upwelling at 60–100 km is manifested in the upward deflection of the tertiary ozone layer by 10 km. This upwelling rapidly cools the region and brings mesospheric air, poor in atomic H, to the altitude of the secondary maximum, where the composite shows a tendency for the nighttime secondary ozone to increase around the time of SSW onset.

[42] The behavior of the simulated secondary ozone layer during SSWs follows the chemical equilibrium assumption in the secondary maximum. The noted intensification of the secondary ozone maximum is consistent with SABER observations. This ozone enhancement is intimately tied to the mesospheric upwelling during the SSW. As suggested by the nighttime equilibrium relationship for ozone, the increase in nighttime ozone mixing ratio is attributed mainly to enhanced cooling due to upwelling and, to a lesser extent, the associated low H. This ozone enhancement ends abruptly with enhanced downwelling during the SSW recovery phase, which adiabatically warms the secondary ozone layer and increases the H mixing ratio.

[43] While atmospheric temperature and H contribute to the equilibrium distribution of nighttime ozone in the MLT, NO_x, with consideration of horizontal transport and solar activity, may play an important role as an indicator of vertical residual motion. In the composite, the warming in the stratosphere (SSW) is accompanied by adiabatic cooling in the mesosphere (SMC); the latter is related to anomalous upwelling due to changes in gravity wave drag, which in turn are caused by the stratospheric wind reversal. In addition to w^* profiles, the evolution of O and H also provide evidence for enhanced polar downwelling and upwelling in association with stratopause layer displacement. These behaviors are largely consistent with the individual ES-SSW cases simulated in the model. The present study summarizes the effect of chemistry and dynamics on MLT ozone during SSWs as revealed by the WACCM4 chemistry-climate model.

[44] **Acknowledgments.** OVT and VL were supported by the National Science Foundation (NSF) under grants AGS-1116123 and AGS-MRI-0958616 and the South Carolina NASA Space Grant. YOR was supported by the Norwegian Research Council through the Norwegian Antarctic Research Programme (prject ES475961). The CESM project is supported by the National Science Foundation and the Office of Science (BER) of the U.S. Department of Energy. CER was supported by NASA LWS grant NNX10AQ54G. Computing resources were provided by the Climate Simulation Laboratory at NCAR's Computational and Information Systems Laboratory (CISL), sponsored by the National Science Foundation and other agencies. NCAR is sponsored by the NSF. The computing assistance of Professor Michael Murphy of CCU's Computer Science department has been invaluable to the completion of this work. We are indebted to the useful comments of Professor Matthew Hitchman and other anonymous reviewers who helped to significantly improve the manuscript.

References

Chandran, A., R. L. Collins, R. R. Garcia, D. R. Marsh, V. L. Harvey, and J. Yue (2013a), A climatology of elevated stratopause events in the Whole Atmosphere Community Climate Model, *J. Geophys. Res. Amos.*, *118*, 1234–1246, doi:10.1002/jgrd.50123.

Chandran, A., R. R. Garcia, R. L. Collins, and L. C. Chang (2013b), Secondary planetary waves in the middle and upper atmosphere following the stratospheric sudden warming event of January 2012, *Geophys. Res. Lett.*, *40*, 1861–1867, doi:10.1002/grl.50373.

De la Torre, L., R. R. Garcia, D. Barriopedro, and A. Chandran (2012), Climatology and characteristics of stratospheric sudden warmings in the Whole Atmosphere Community Climate Model, *J. Geophys. Res.*, *117*, D04110, doi:10.1029/2011JD016840.

Hitchcock, P., and T. G. Shepherd (2012), Zonal mean dynamics of the Arctic polar-night jet oscillation, *J. Atmos. Sci.*, doi:10.1175/JAS-D-12-0111.1.

Hitchman, M. H., J. C. Gille, C. D. Rodgers, and G. Brasseur (1989), The separated polar winter stratopause: A gravity wave driven climatological feature, *J. Atmos. Sci.*, *46*, 4310–4422.

Hoffmann, C. G., D. E. Kinnison, R. R. Garcia, M. Palm, J. Notholt, U. Raffalski, and G. Hochschild (2012), CO at 40–80 km above Kiruna observed by the ground-based microwave radiometer KIMRA and simulated by the Whole Atmosphere Community Climate Model, *Atmos. Chem. Phys.*, *12*, 3261–3271.

Holton, J. R. (1976), A semi-spectral numerical model for wave-mean flow interactions in the stratosphere. Application to the sudden stratospheric warmings, *J. Atmos. Sci.*, *33*, 1639–1649.

Karlsson, B., C. McLandress, and T. G. Shepherd (2009), Inter-hemispheric mesospheric coupling in a comprehensive middle atmosphere model, *J. Atmos. Sol. Terr. Phys.*, *71*, 518–530, doi:10.1016/j.jastp.2008.08.006.

Kunz, A., L. Pan, P. Konopka, and D. Kinnison, S. Tilmes (2011), Chemical and dynamical discontinuity at the extratropical tropopause based on START08 and WACCM analysis, *J. Geophys. Res.*, *116*, D24302, doi:10.1029/2011JD016686.

Kuroda, Y. (2008), Effect of stratospheric sudden warming and vortex intensification on the tropospheric climate, *J. Geophys. Res.*, *113*, D15110, doi:10.1029/2007JD009550.

Kvissel, O.-K., Y. J. Orsolini, F. Stordal, V. Limpasuvan, J. H. Richter, and D. R. Marsh (2012), Mesospheric intrusion and anomalous chemistry during and after a major stratospheric sudden warming, *J. Atmos. Sol. Terr. Phys.*, *78-79*, 116–124, doi:10.1016/j.jastp.2011.08.015.

Labitzke, K. (1981), Stratospheric-mesospheric midwinter disturbances: A summary of characteristics, *J. Geophys. Res.*, *86*, 9665–9678, doi:10.1029/JC086iC10p09665.

Lee, J. N., D. L. Wu, G. L. Manney, M. J. Schwartz, A. Lambert, N. J. Livesey, K. R. Minschwaner, H. C. Pumphrey, and W. G. Read (2011), Aura microwave limb sounder observations of the polar middle atmosphere: Dynamics and transport of CO and H_2O, *J. Geophys. Res.*, *116*, D05110, doi:10.1029/2010JD014608.

Limpasuvan, V., D. W. J. Thompson, and D. L. Hartmann (2004), The life cycle of Northern Hemisphere sudden stratospheric warmings, *J. Climate*, *17*, 2584–2596.

Limpasuvan, V., D. L. Hartmann, D. W. J. Thompson, K. Jeev, and Y. L. Yung (2005), Stratosphere-troposphere evolution during polar vortex intensification, *J. Geophys. Res.*, *110*, D24101, doi:10.1029/2005JD006302.

Limpasuvan, V., J. H. Richter, Y. J. Orsolini, F. Stordal, and O.-K. Kvissel (2012), The roles of planetary and gravity waves during a major stratospheric sudden warming as characterized in WACCM, *J. Atmos. Sol. Terr. Phys.*, *78-79*, 84–98, doi:10.1016/j.jastp.2011.03.004.

Manney, G. L., K. Krüger, S. Pawson, M. J. Schwartz, W. H. Daffer, N. J. Livesey, M. G. Mlynczak, E. E. Remsberg, J. M. Russell III, and J. W. Waters (2008), The evolution of the stratopause during the 2006 major warming: Satellite data and assimilated meteorological analyses, *J. Geophys. Res.*, *113*, D11115, doi:10.1029/2007JD009097.

Marsh, D.R., A.K. Smith, G. Brasseur, G. M. Kaufmann, and K. Grossmann (2001), The existence of a tertiary ozone maximum in the high-latitude middle mesosphere, *Geophys. Res. Lett.*, doi:10.1029/2001GL013791.

Marsh, D. R. (2011), Chemical-dynamical coupling in the mesosphere and lower thermosphere, *Aeronomy of the Earth's Atmosphere and Ionosphere*, M. Ali Ali Abdu and D. Pancheva, pp. 3–17, eds. Springer, New York, NY.

Matsuno, T. (1971), A dynamical model of the stratospheric sudden warming, *J. Atmos. Sci.*, *28*, 1479–1494 doi:10.1175/1520-0469.

McLandress, C., J. F. Scinocca, T. G. Shepherd, M. C. Reader, and G. L. Manney (2012), Dynamical control of the mesosphere by orographic and non-orographic gravity wave drag during the extended northern winters of 2006 and 2009, *J. Atmos. Sci.*, doi:10.1175/JAS-D-12-0297.1.

Orsolini, Y. J., J. Urban, D. P. Murtagh, S. Lossow, and V. Limpasuvan (2010), Descent from the polar mesosphere and anomalously high stratopause observed in 8 years of water vapor and temperature satellite observations by the ODIN sub-millimeter radiometer, *J. Geophys. Res.*, *115*, D12305, doi:10.1029/2009JD013501.

Randall, C. E., et al. (2005), Stratospheric effects of energetic particle precipitation in 2003–2004, *Geophys. Res. Lett.*, *32*, L05802, doi:10.1029/2004GL02203.

Randall, C. E., V. L. Harvey, C. S. Singleton, P. F. Bernath, C. D. Boone, and J. U. Kozyra (2006), Enhanced NO_x in 2006 linked to strong upper stratospheric Arctic vortex, *Geophys. Res. Lett.*, *33*, L18811, doi:10.1029/2006GL027160.

Randall, C. E., V. L. Harvey, D. E. Siskind, J. France, P. F. Bernath, C. D. Boone, and K. A. Walker (2009), NO_x descent in the Arctic middle atmosphere in early 2009, *Geophys. Res. Lett.*, *36*, L18811, doi:10.1029/2009GL039706.

Rienecker, M. M., et al. (2011), MERRA: NASA's modern-era retrospective analysis for research and applications, *J. Climate*, *24*, 3624–3648, doi:10.1175/JCLI-D-11-00015.1.

Siskind, D. E., L. Coy, and P. Espy (2005), Observations of stratospheric warmings and mesospheric coolings by the TIMED SABER instrument, *Geophys. Res. Lett.*, *32*, L09804, doi:10.1029/2005GL022399.

Siskind, D. E., S. D. Eckermann, L. Coy, J. P. McCormack, and C. E. Randall (2007), On recent interannual variability of the Arctic winter mesosphere: Implications for tracer descent, *Geophys. Res. Lett.*, *34*, L09806, doi:10.1029/2007GL029293.

Siskind, D. E., S. D. Eckermann, J. P. McCormack, L. Coy, K. W. Hoppel, and N. L. Baker (2010), Case studies of the mesospheric response to recent minor, major, and extended stratospheric warmings, *J. Geophys. Res.*, *115*, D00N03, doi:10.1029/2010JD014114.

Smith, A. K., and D. R. Marsh (2005), Processes that account for the ozone maximum at the mesopause, *J. Geophys. Res.*, *110*, D23305, doi:10.1029/2005JD006298.

Smith, A. K. (2012), Global dynamics in MLT, *Surv. Geophys.*, 54, doi:10.1007/s10712-012-9196-9.

Smith, A. K., D. R. Marsh, J. M. Russell III, M. G. Mlynczak, F. J. Martin-Torres, and E. Kyrola (2008), Satellite observations of high nighttime ozone at the equatorial mesopause, *J. Geophys. Res.*, *113*, D17312, doi:10.1029/2008JD010066.

Smith, A. K., M. Lopez-Puertas, M. Garcia-Comas, and S. Tukiainen (2009), SABER observations of mesospheric ozone during NH late winter 2002–2009, *Geophys. Res. Lett.*, *36*, L23804, doi:10.1029/2009GL040942.

Smith, A. K., D. R. Marsh, M. G. Mlynczak, and J. C. Mast (2010), Temporal variations of atomic oxygen in the upper mesosphere from SABER, *J. Geophys. Res.*, *115*, D18309, doi:10.1029/2009JD013434.

Smith, A. K., R. R. Garcia, D. R. Marsh, and J. H. Richter (2011), WACCM simulations of the mean circulation and trace species transport in the winter mesosphere, *J. Geophys. Res.*, *116*, D20115, doi:10.1029/2011JD016083.

Sonnemann, G. R., M. Grygalashvyly, and U. Berger (2006), Impact of a stratospheric warming event in January 2001 on the minor constituents in the MLT region calculated on the basis of a new 3-D-model LIMA of the dynamics and chemistry of the middle atmosphere, *J. Atmos. Sol. Terr. Phys.*, *68*, 2012–2025.

SPARC (2010), Ccmval 2010: Sparc report on the evaluation of chemistry climate mod-814 els. WCRP-132, WMO/TD1526. (SPARC Report No. 5), URL http://www.815 sparc-climate.org/publications/sparc-reports/.

Taylor, J. R. (1997), *An Introduction to Error Analysis*, 2nd ed., pp. 166–168, University Science Books, Sausalito, California.

Tomikawa, Y., K. Sato, S. Watanabe, Y. Kawatani, K. Miyazaki, and M. Takahashi (2012), Growth of planetary waves and the formation of an elevated stratopause after a major stratospheric sudden warming in a T213L256 GCM, *J. Geophys. Res.*, *117*, D16101, doi:10.1029/2011JD017243.